

Triboelectric–Pyroelectric–Piezoelectric Hybrid Cell for High-Efficiency Energy-Harvesting and Self-Powered Sensing

Yunlong Zi, Long Lin, Jie Wang, Sihong Wang, Jun Chen, Xing Fan, Po-Kang Yang, Fang Yi, and Zhong Lin Wang*

Due to the world-wide fast raising demands in energy, more and more efforts have been dedicated to looking for sustainable energy sources. On the other hand, with the rapid development of the portable and wearable electronics, there is a huge demand of energy harvesting from ambient environment for these devices and systems.^[1,2] As one of the most commonly available energies in the environment, mechanical energy has been used for a long time by converting itself into electrical energy through generators, such as electromagnetic generators (EMG), piezoelectric nanogenerators (PENG),^[3–5] and triboelectric nanogenerators (TEG).^[6–8] Among them, triboelectric nanogenerators have shown advantages of high output power, high energy conversion efficiency, low cost, and abundant choices of materials.^[7] Despite these advantages, the energy conversion efficiency of the TEG may still be limited by the energy loss during the power generation process. Take the sliding TEG as an example, substantial amount of energy input will be wasted through friction induced heat dissipation, especially for the high-frequency sliding motion; besides, the work done by the indispensable normal force applied on the contact surface will result in additional energy loss. In this regard, high-efficient nanogenerators have been developed based on noncontact approach^[9,10] to minimize the energy loss in the friction; from another point of view, it is also reasonable to fully scavenge the lost energy by hybridizing supplementary power generators. Here, pyroelectric nanogenerators can be employed for harvesting the thermal energy from the friction-induced temperature fluctuation, and piezoelectric nanogenerators can harvest the mechanical energy from the small deformation of materials caused by the normal force.

At the same time, various environmental factors, for example, high temperature or high normal force during the friction, can impact the stability of the frictional motion. Working in the extreme conditions may also result in failures of the sensor units. Conventional sensors for detecting these environmental parameters require additional power supply, which is a huge limitation for minimizing the sensors and decreasing environmental-unfriendly waste materials from the

batteries. Thus, the hybrid cell equipped in the frictional units that is able to work not only as a high-efficient energy-harvester, but also as a self-powered sensor is highly desirable.

Here, we reported a triboelectric–pyroelectric–piezoelectric hybrid cell composed of a sliding mode TENG and a pyroelectric–piezoelectric nanogenerator (PPENG) with outstanding performances. By harvesting the majority of the mechanical energy during the sliding motion, the TENG with a size of 63.5 cm² has produced an area power density of 0.15 W m⁻² at a sliding frequency of 4.41 Hz. The PPENG is able to harvest the thermal energy of the friction-induced heat and the mechanical energy induced by the normal force. The hybrid cell has been demonstrated to extend the illumination time of a LED and charge a supercapacitor at a charging rate about twice of that charged by the TENG alone. This hybrid cell has also been demonstrated as a self-powered temperature and normal force sensor during the frictional motion. These outstanding performances demonstrate the hybrid cell as a promising energy harvester and self-powered sensor for future applications.

As shown in **Figure 1a**, the hybrid cell has a multilayered planar structure composed of a sliding-mode TENG on the top and a PPENG on the bottom. In the TENG, a layer of aluminum (Al) foil was used as the sliding part and a piece of polytetrafluoroethylene (PTFE) film deposited with copper (Cu) electrode was utilized as the static part. For the PPENG, a piece of 110 μm-thick polarized polyvinylidene fluoride (PVDF) deposited with Cu electrodes on both sides was attached underneath the TENG. A Kapton film was laminated between the bottom electrode of the TENG and the top electrode of the PPENG as an electronically insulating but thermally conductive layer. The heights of both the sliding and static parts were adjusted to ensure that the Al foil and the PTFE film contact firmly and keep aligned during the sliding. The motion of the Al foil was controlled by a linear motor to slide on the PTFE surface periodically with a period of 0.2267 s and a displacement of 80 mm. The total frictional area was determined to be 63.5 cm². A thermocouple was placed in the center of the frictional area underneath the bottom side of the PPENG to record the temperature variation.

The operation and theoretical study of the sliding mode TENG have been reported previously.^[11–13] As shown in **Figure 1b**, the working principle of the TENG is based on the coupling of triboelectrification and electrostatic induction. Specifically, upon the contact/friction between the two parts of the TENG, the Al layer is positively charged, while the surface of PTFE gets negatively charged due to their distinct surface polarities.^[7] The net negative charges on the PTFE are immobile and tend to preserve for a long period of time considering the insulating nature of the electret polymer material. Once the Al foil is

Dr. Y. Zi, L. Lin, Dr. J. Wang, Dr. S. Wang, J. Chen
Dr. X. Fan, P.-K. Yang, F. Yi, Prof. Z. L. Wang
School of Materials Science and Engineering
Georgia Institute of Technology
Atlanta, GA 30332-0245, USA
E-mail: zlwang@gatech.edu

Prof. Z. L. Wang
Beijing Institute of Nanoenergy and Nanosystems
Chinese Academy of Sciences
Beijing 100083, P.R. China



DOI: 10.1002/adma.201500121

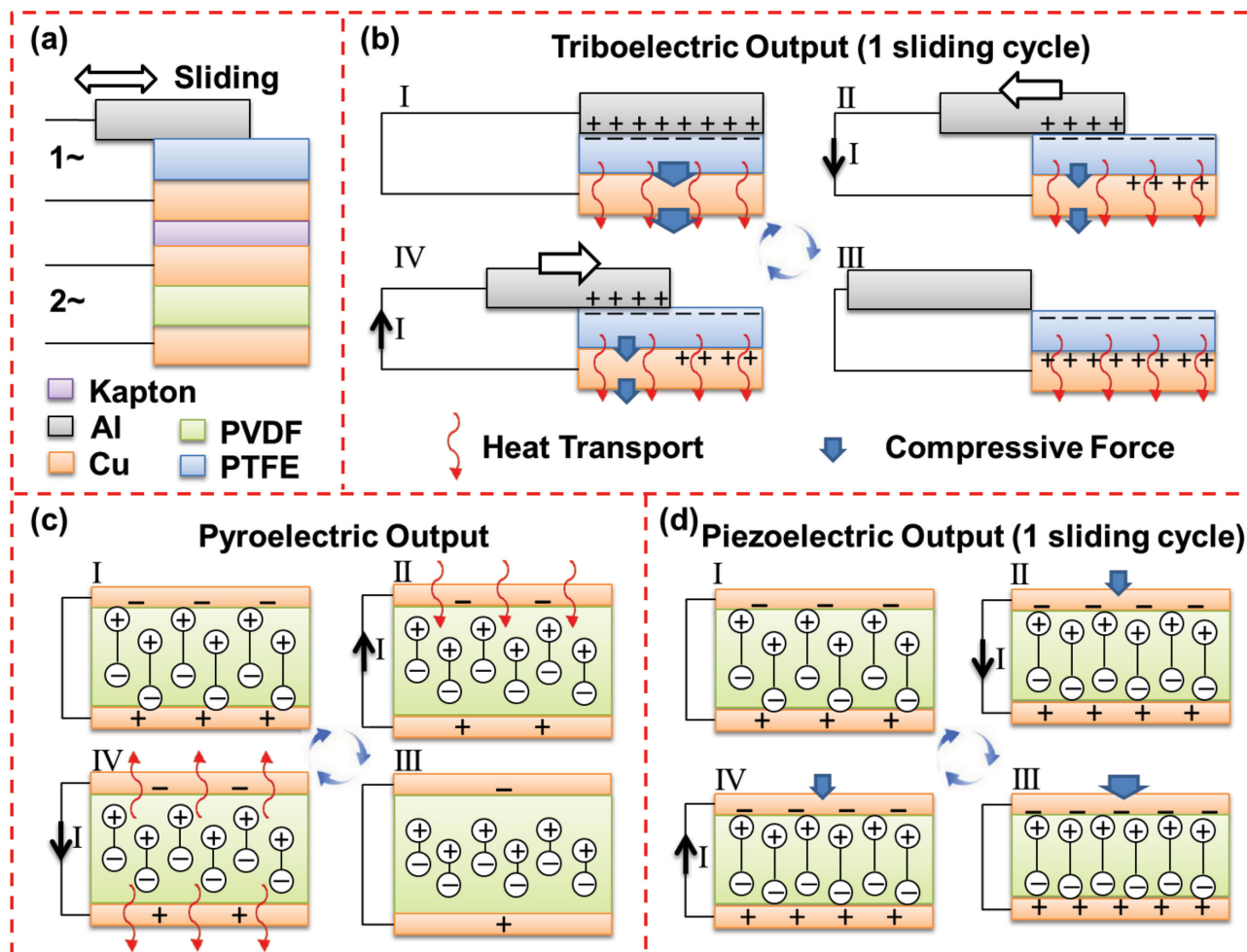


Figure 1. The structure and working mechanism of the hybrid cell. a) The structure of the hybrid cell, where 1 is the output from triboelectric nanogenerator (TENG) and 2 is the output from pyroelectric–piezoelectric nanogenerator (PPENG); b) the working mechanism of the output in TENG; c,d) the working mechanism of the pyroelectric and the piezoelectric outputs in PPENG, respectively.

sliding away from the aligned position, the separation of triboelectric charges on both surfaces leads to potential difference between the Al and Cu electrodes. This potential difference is represented as the voltage in the open-circuit condition, and serves as the driving force for the charge flow in the short-circuit condition (Figure 1b-II), until the Al foil fully slides away from the top of the PTFE film (Figure 1b-III). When the Al foil is moving back, the open-circuit potential difference drops and the electrons flow back in the short-circuit condition to reach equilibrium (Figure 1b-IV). Eventually, the Al foil goes back to the aligned position to complete one sliding circle (Figure 1b-I).

The operation of the PPENG highly depends on the performance of the polarized PVDF film. The detailed mechanisms of the piezoelectric and pyroelectric effects in PVDF are explained in the Supporting Information, which have been reported previously.^[14–20] Figure 1c,d explain the pyroelectric and piezoelectric outputs of the PPENG, respectively. In the device structure, the PVDF in PPENG is placed with the polarization direction upward (Figure 1c-I,d-I). During the periodical sliding motion, the underlying PVDF film undergoes a normal force and receives the heat induced by the

friction. With the increase of the temperature due to the friction induced heat, as we discussed in the Supporting Information, the dipole moments decrease and the volume expands, both of which reduce the polarization density. To balance the extra charges owing to the reduction of the polarization density, a negative potential difference from the top to the bottom electrodes is created across the PVDF under open-circuit condition, and a current is driven to flow from the bottom electrode to the top electrode of the PVDF (Figure 1c-II) in the short-circuit condition. After the sliding motion stops (Figure 1c-III), the heat dissipation from the PVDF film leads to the increase of the polarization density, which reduces the absolute value of the potential difference in the open-circuit condition, and drives the current flow in the reverse direction in the short-circuit condition (Figure 1c-IV). The open-circuit voltage and short-circuit current owing to the pyroelectric effect can be derived as^[19,21]

$$V = \frac{A\Delta\sigma}{C} = \frac{A}{A'} \times \frac{\Delta\sigma d}{\epsilon_r \epsilon_0} = \frac{A}{A'} \times \frac{d}{\epsilon_r \epsilon_0} p\Delta T \quad (1)$$

$$I = \frac{d(\sigma A)}{dt} = pA \frac{dT}{dt} \text{ or } \Delta Q = \int Idt = pA\Delta T \quad (2)$$

Here, d , A' , and C are the thickness, the total area, and the capacitance of the PVDF in PPENG, respectively. A is the frictional area, which is considered to be the thermally affected area in PVDF. p and ϵ_r are the pyroelectric coefficient and the relative dielectric constant of the PVDF, respectively, and ϵ_0 is the permittivity of the vacuum. V , ΔQ , ΔT , and I represent the open-circuit voltage, the transferred charge, the temperature variation, and the current, respectively. Since the polarization direction is perpendicular to the film plane, we can consider the charge density variation as $\Delta\sigma = \Delta P = p\Delta T$.^[22] Unlike other common pyroelectric materials such as PZT and ZnO, the open-circuit condition of PVDF could be achieved easily due to its high resistivity (Table S1, Supporting Information), which ensures the proportional relationship between V and ΔT in Equation (1). The recorded open-circuit voltage and short-circuit current of the PPENG subject to the temperature variation are shown in Figure S1, Supporting Information, showing that the open-circuit voltage is proportional to the temperature variation and the short-circuit current is proportional to the temperature changing rate (dT/dt), which are consistent with Equations (1) and (2), respectively.

When the sliding part moves in, the normal compressing force is applied on the PVDF film, resulting in a negative strain and reduced volume of the PVDF film. Thus, the polarization density is enhanced and the current flows from the top electrode to the bottom electrode to balance the extra polarization density (Figure 1d-II) in the short-circuit condition. In the aligned position of the TENG, the largest normal force is achieved (Figure 1d-III). When the sliding part slides out, the applied

force decreases and then the current flows back to balance the charge induced by the release of the strain (Figure 1d-IV) in the short-circuit condition. The open-circuit voltage and the short-circuit transferred charge owing to the piezoelectric effect have been derived to be proportional to the applied normal force.^[23] Compared to the pyroelectric effect, the piezoelectric effect is considered to be more complex since all of the 3D strains can affect the polarization density.

The performance of the TENG was measured while the Al foil was sliding periodically. For the open-circuit voltage as shown in Figure 2a, it oscillated with a peak-to-peak value of 1132.6 V. In the short-circuit condition, the current density was measured to be an AC output with a peak value of 1.45 mA m^{-2} ($9.2 \text{ } \mu\text{A}$ in the current peak) as shown in Figure 2b. Both the voltage and the current were measured to have the same period as that of the sliding motion. These results are comparable to previously reported values.^[11,12] To determine the optimized load resistance and the maximum power density outputs, the external loads with different resistances were applied. As the load resistance increased, the amplitudes of the output current peaks were observed to drop and the voltage peak values were observed to be enhanced (Figure 2c). Then the peak power densities corresponding to load resistances were calculated as the product of the corresponding current and voltage (Figure 2d). The maximum peak power density was determined as 146.2 mW m^{-2} at the matched load of $140 \text{ M}\Omega$. As demonstrated in prior works of sliding-mode TENG with similar dimensions and materials, the energy conversion efficiency has been estimated to be about 8%–31%.^[11,12] The output performance of the sliding-mode TENG could be further enhanced through advanced structural designs such as the micrograted structure^[12,24] and the rotational disk structure,^[25] which opens

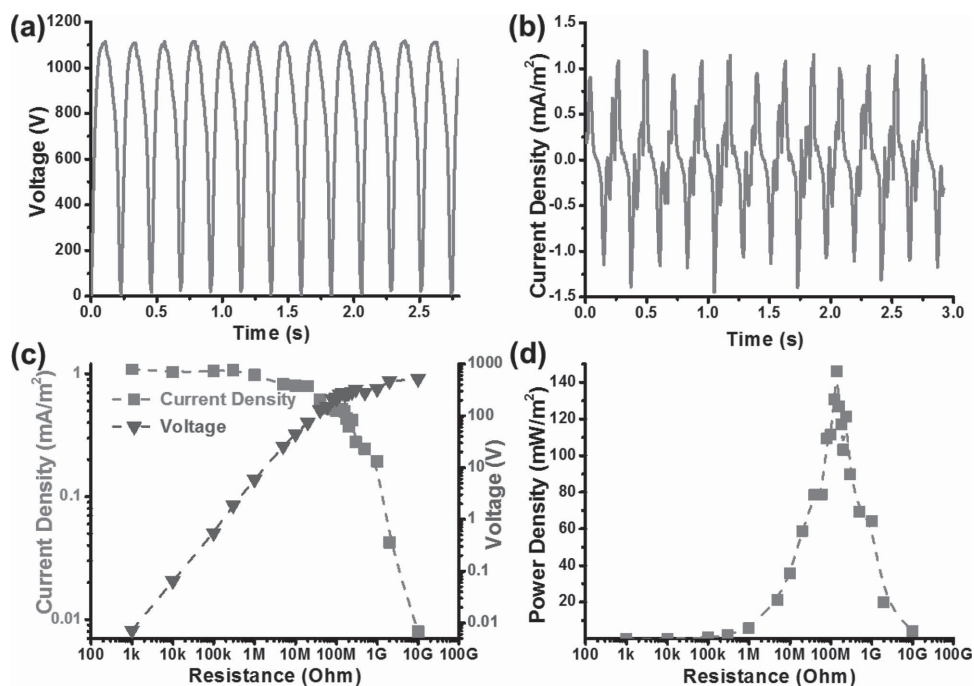


Figure 2. Electrical characterization of the triboelectric nanogenerator (TENG). a) The open-circuit voltage of the TENG; b) The short-circuit current density of the TENG; c) The voltage and current density peak values with external load resistances applied; d) The power density of the TENG with different load resistances.

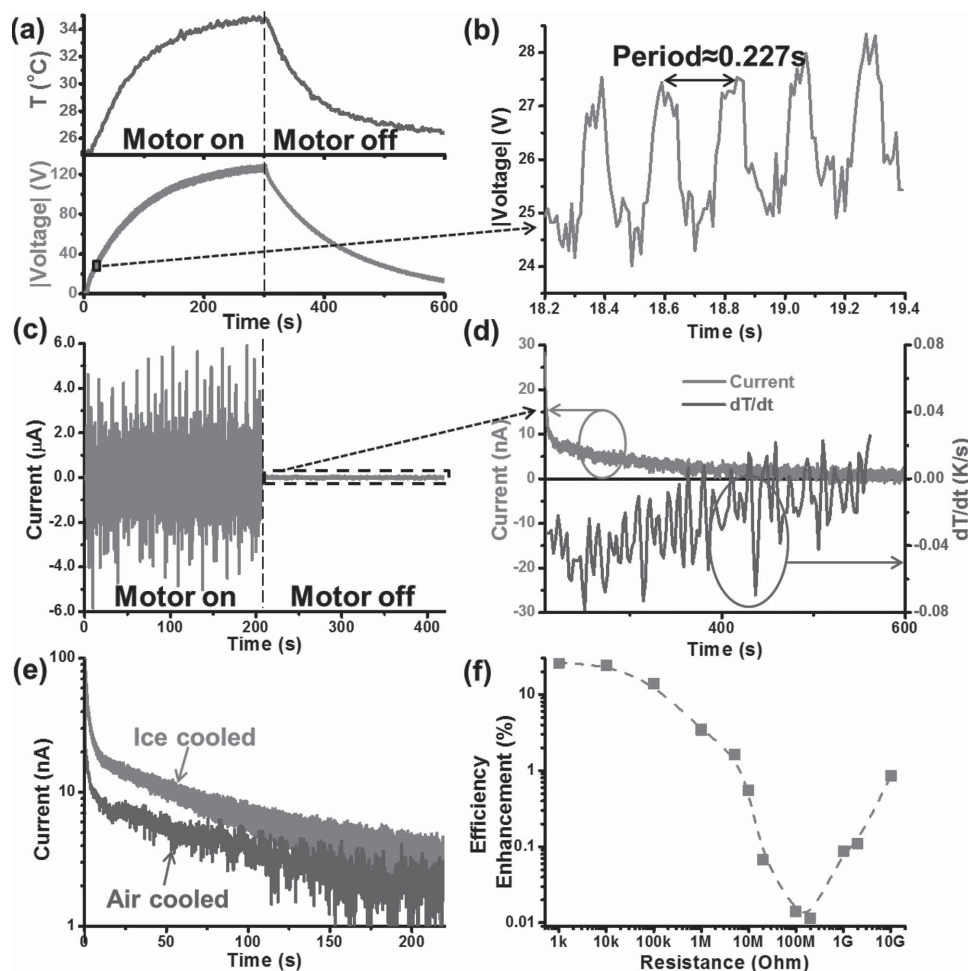


Figure 3. Electrical characterization of the pyroelectric–piezoelectric nanogenerator (PPENG). a) The open-circuit voltage variation and the temperature of the PPENG (circled area is shown in (b)). The voltage between the top and bottom electrodes decreased when temperature increased; b) When the motor was on, a detailed view of the voltage variation showing the oscillating piezoelectric voltage; c) The short-circuit current of the PPENG (area circled by the dashed line is shown in (d)); d) The pyroelectric current and temperature changing rate dT/dt after the motor was off; e) The enhanced pyroelectric current by the ice cooling compared with the one cooled in air; f) The enhancement of the energy-harvesting efficiency of the hybrid cell compared with that of only the TENG subject to various external load resistances.

up possibilities for its practical applications in high-efficient and large scale energy harvesting.

The performance of the PPENG was measured in the entire range of the sliding motion (motor on) and after the sliding motion stopped (motor off). The open-circuit voltage variation between the top and the bottom electrodes was first measured as shown in Figure 3a. When the motor was on, the voltage became negative, and the voltage decreasing rate was high initially and then approached to zero gradually. After the motor was off, the voltage increased back to zero gradually. To clarify the origin of this voltage signal, the temperature variation of the PPENG in the entire process was measured, also as shown in Figure 3a. We noticed that the main part of the voltage decrease is proportional to the temperature increase, which was consistent with the linear relationship between V and ΔT in Equation (1) and the fact of the negative pyroelectric coefficient p .^[18] This result indicated that the majority of the open-circuit voltage variation was due to the pyroelectric effect from the temperature variation, as a result of the friction-induced heat.

We also observed when the motor was on, there were periodical oscillations of about 3 V in the voltage (Figure 3b); as a comparison, after the motor was off, the voltage became relatively smooth without periodical oscillations (Figure S2a, Supporting Information). Thus, these oscillations were determined to come from the piezoelectric effect induced by the periodically applied normal force. This normal force was estimated experimentally as about 4.1 N (see the Supporting Information). The period of the voltage oscillations was measured as about 0.227 s, which was consistent with the period of the sliding motion.

The short-circuit current was measured as an AC output when the motor was on (Figure 3c) and a decreasing unidirectional positive output after the motor was off (Figure 3c,d). Due to Equation (2), the pyroelectric short-circuit current was proportional to the changing rate of the temperature dT/dt . The temperature kept increasing when the motor was on and decreasing after the motor was off, as a result, the pyroelectric part of the current should be negative when the motor was on and positive after the motor was off, respectively. At the same

time, the normal force was applied periodically only when the motor was on, resulting in an AC output as the piezoelectric part of the current. While the motor was on, it was reasonable to determine the majority of the measured AC output (larger than 10^{-6} A) as the piezoelectric current, since the normal force changed frequently (in the period of 0.2267 s), resulting in a large dF/dt as well as a larger piezoelectric current than the pyroelectric current (estimated as only about 10^{-8} A level). After the motor was off, there was only unidirectional current existed decaying from about 3×10^{-8} A. To verify it was the pyroelectric current, we measured the temperature variation and calculated the changing rate of the temperature dT/dt , as plotted in Figure 3d. Even though there was a large noise level in the dT/dt curve, the negative dT/dt was still observed to be approaching zero, which was consistent with the variation of the current. Therefore, this measured unidirectional current was confirmed as the pyroelectric current. Here, the effects from the TENG could be excluded, since the charge interaction between the TENG and the PPENG was determined to be negligible, as stated in the Supporting Information.

In order to enhance the short-circuit pyroelectric current after the motor was off, we repeated the experiment with a box of ice inserted just right below the device while the motor was turning off. In the open-circuit voltage and the temperature measurement, we observed that both the voltage and the temperature recovered in a shorter time (Figure S2b, Supporting Information). In the short-circuit condition, the initial pyroelectric current was enhanced to be about 1×10^{-7} A (Figure 3e). The temperature decreasing rate dT/dt was also observed to be enhanced to be about twice or even more times (Figure S2c, Supporting Information).

It can be found from the above measurement results that the PPENG can convey a high short-circuit current from the piezoelectric effect, and a high open-circuit voltage from the pyroelectric effect. Hence, the overall PPENG output was hybridized by pyroelectric and piezoelectric outputs with the ratio between them tuned by the external load resistance. With large load resistances (≥ 60 M Ω), the output profile of the PPENG was measured to be mainly the pyroelectric output, which is related to the temperature variation, at the same time the oscillations from the piezoelectric effect could still be observed while the motor was on (Figure S2d, Supporting Information). With small load resistances (<60 M Ω), the output profile was measured to be mainly the AC output from the piezoelectric

effect (Figure S2e, Supporting Information). The average power densities of the PPENG and the TENG subject to various load resistances were calculated (see the Supporting Information for the calculation method and Figure S2f, Supporting Information, for the calculated PPENG average power density), and then the ratio between the average power densities of the PPENG and the TENG was calculated as the enhancement of the energy-harvesting efficiency of the hybrid cell compared with that of the TENG only (Figure 3f). This efficiency enhancement was found to be larger than 10% subject to small load resistances (≤ 100 k Ω), and it could reach up to 26.2% with the load resistance of 1 k Ω . With proper operations or power management designs, the overall output could be further optimized and implemented in broader applications.

By using Equation (1) and the integral form of Equation (2), the pyroelectric coefficient p was calculated as -1.80 ± 0.07 nC cm $^{-2}$ K $^{-1}$. It was noticed that the absolute value of the coefficient calculated here was smaller than the one calculated in the pyroelectric measurement in the Supporting Information. The reason is that the temperature range we measured here was about 25–35 °C while the range measured in the Supporting Information was about 44–50 °C. It has been reported that around room temperature, the absolute value of the pyroelectric coefficient of PVDF becomes larger under a higher temperature.^[26]

By using rectifiers, both the output currents from the TENG and PPENG could be converted to be unidirectional. The output performances from both the TENG and PPENG were hybridized by connecting the two rectified output currents in parallel (Figure 4a). The hybridized output current was measured, as shown in Figure 4b, which was up to 10^{-5} A level when the motor was on. This hybridized output was utilized to power up a LED bulb first. When the motor was on, the LED was turned on with a strong illumination intensity (left inset of Figure 4b); as soon as the motor was off, the LED turned off gradually since the pyroelectric output current enabled the illumination in a lower intensity (right inset of Figure 4b). This phenomenon was not observed in the LED driven by only the rectified TENG output. It was also demonstrated that this hybridized output could charge a supercapacitor with a high capacitance (C) of 41.9 mF. The voltage across the supercapacitor during charging was plotted in Figure 4c. As comparison, the voltages across the supercapacitor charged by only the rectified TENG and PPENG outputs were also plotted, respectively. It was

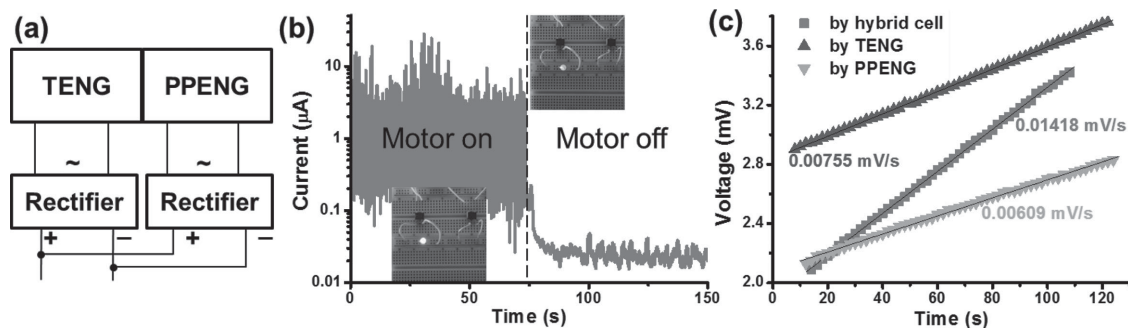


Figure 4. The output performance of the hybrid cell. a) The circuits to hybridize the outputs from TENG and PPENG; b) The hybridized output current, with the LED lighted by the hybridized output when the motor was on and after the motor was off, as shown in insets; c) The voltages of the supercapacitor charged by the hybridized output, the rectified TENG and PPENG outputs of the hybrid cell when the motor was on.

observed that the supercapacitor could be charged faster by the hybridized output than that by only one individual output. The charging rate by the hybridized output was about the sum of the charging rates of the rectified TENG and PPENG outputs. The average value of the charging current could be calculated by the following equation

$$\bar{I} = \frac{dQ}{dt} = C \frac{dV}{dt} \quad (3)$$

When the motor was on, the average charging currents of the hybrid cell, the rectified TENG and the rectified PPENG outputs were calculated as about 0.59, 0.32, and 0.26 μA , respectively.

The structure of the hybrid cell was able to not only work for hybrid energy harvesting, but also work as a self-powered sensor of the temperature and the normal force applied on the surface that undergoes friction. The advantages of using PVDF in the PPENG as the sensor were discussed in the Supporting Information. To better illustrate the temperature sensing performance, the hybrid cell structure was modified to be a rotation-based structure. In this structure, three identical PPENGs with a size of 4 cm^2 were laminated between a layer of the PTFE film and disc 2 in Figure 5a. The positions of the PPENGs were in the side (#1), in the half-radius (#2), and in the center of the disc

(#3), respectively, which would experience different temperature increases during the identical rotational friction. The PTFE film on the disc 2 was used as one frictional surface, and a layer of Al foil was attached on the disc 1 as the other frictional surface. The rotation rate of the disc 1 was set to be 500 rpm driven by a rotational motor, and different levels of voltage drops in the three PPENGs were observed during the rotation (Figure 5c). The temperature of PPENG #1 was measured by inserting a thermocouple between PPENG #1 and the rotation disc 2, as plotted in Figure 5b. The temperature variations in PPENG #2 and #3 were too small to be measured by the thermocouple. It was observed that the temperature variation was proportional to the voltage drops, which was consistent with our previous results. By using Equation (1) ($A = A'$ right now) and assuming pyroelectric coefficient $p = -1.80 \text{ nC cm}^{-2} \text{ K}^{-1}$ as we previously calculated, the temperature increase of the PPENG #1 during 128 s of the rotation was calculated as about 0.99 $^{\circ}\text{C}$, which was consistent with the temperature variation measured by the thermocouple (Figure 5b). Similarly, the temperature increases of the PPENG #2 and #3 were calculated as only about 0.22 and 0.09 $^{\circ}\text{C}$, respectively, which were both smaller than the noise level of our thermocouple (about 0.3 $^{\circ}\text{C}$). Therefore, our structure of the hybrid cell could be used as the self-powered temperature sensor with the detection limit far beyond that of the thermocouple.

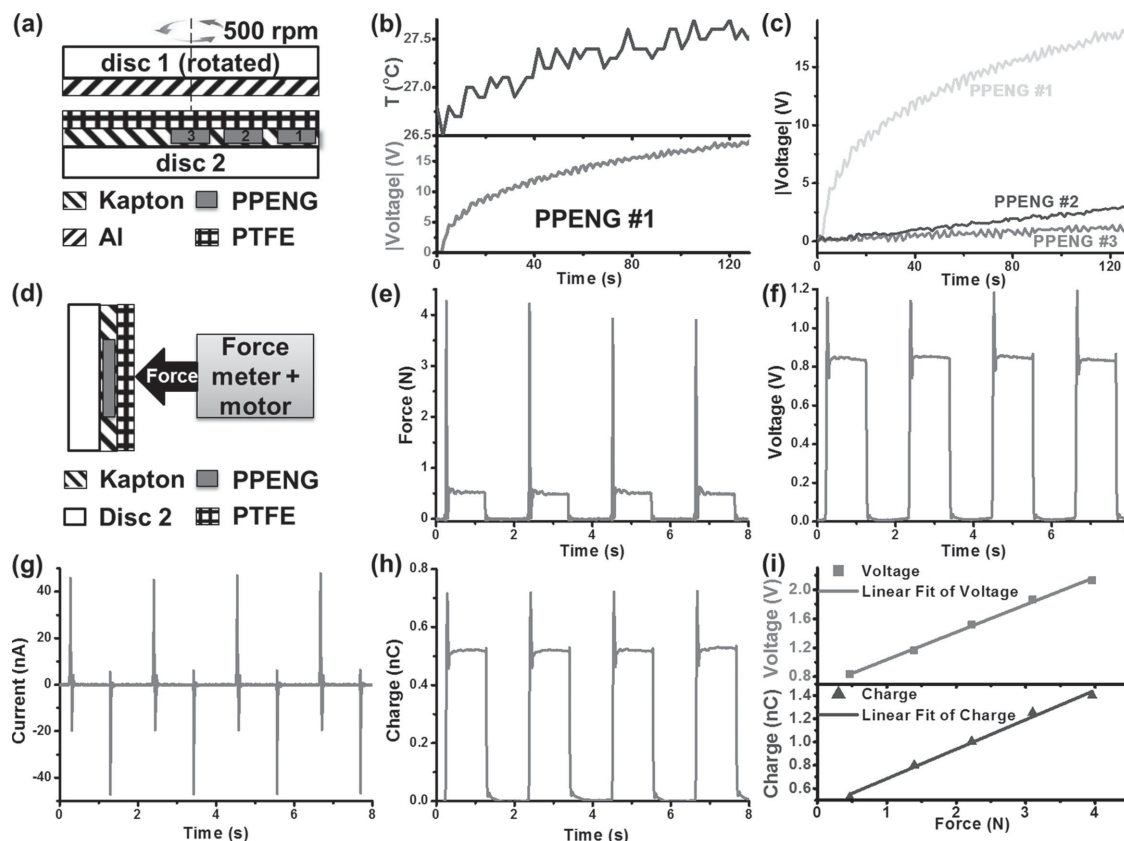


Figure 5. The hybrid cell worked as a self-powered a–c) temperature and d–i) normal force sensor. a) The cross-sectional schematic diagram of the structure used to demonstrate the temperature sensing. The dashed line indicates the axis of the rotation of disc 1; b) the voltage and the temperature variations of the PPENG #1; c) the voltage variations of the PPENG #1–3. d) The schematic diagram of the measurement setup; e) The first force (about 0.5 N) applied on the surface. Please note that the sharp peaks were ignored in calculation (the same for the voltage and the charge in the following plots); f–h) The open-circuit voltage, the short-circuit current, and the transferred charge in PPENG under the force of about 0.5 N applied periodically. i) Plots and the linear fits of the open-circuit voltage and short-circuit transferred charge versus the force.

By utilizing the piezoelectric effect, this hybrid cell structure could also be used as a normal force sensor. To demonstrate the normal force sensing performance, a perpendicular force on the disc 2 was applied and measured by a force meter connected with a linear motor (Figure 5d). Various displacements were controlled by the motor to create several different periodical forces at the same moving velocity. Here, PPENG #3 in the previous section was used as the sensor in our experiment. With periodical forces applied on the surface (Figure 5e), the periodical open-circuit voltage platforms and short-circuit current peaks were recorded (Figure 5f,g). The transferred charge could be calculated as the integral of the measured current (Figure 5h). Here, the results in Figure 5e–h showed the measurement results with the force of about 0.5 N, and only the platform values of the force, voltage, and charge were considered (the sharp peaks were ignored). Subject to different values of the forces, the differences between the higher and the lower platform values of both the open-circuit voltages and the short-circuit transferred charges were plotted (Figure 5i). These two plots were linearly fitted, with the coefficients of determinations R^2 equal to 0.997 for the voltage–force curve and 0.990 for the charge–force curve. It was reasonable to observe the nonzero intercepts, since there were triboelectric charges created during the separation–contact process, which affected the potentials of the electrodes of the PPENG. The good linearity of both the plots demonstrated the hybrid cell as a self-powered sensor for the normal force applied.

In summary, we developed a hybrid cell composed of a TENG and a PPENG to efficiently harvest energy during the friction motion. For the TENG, high oscillating AC outputs with a maximum power density of 146.2 mW m^{-2} were achieved at the sliding frequency of 4.41 Hz. For the PPENG, the main part of the open-circuit voltage was observed to be proportional to the temperature variation. In short-circuit condition, when motor was on, oscillating piezoelectric current was observed; after the motor was off, decaying unidirectional pyroelectric current was observed. With the PPENG integrated on the TENG, the mechanical energy harvesting efficiency enhancement could be up to 26.2%. The hybridized output was demonstrated for instantaneously driving the LED with extended illumination time and charging a supercapacitor in the charging rate about twice of that charged by the TENG only. The structure of the hybrid cell was also demonstrated as a multifunctional self-powered sensor for detecting both the subtle temperature variation and the normal force on the surface. These outstanding performances of the hybrid cell make it a perfect candidate for both power generators and active sensors, which is a substantial advancement in nanogenerators and will push forward its practical applications to a new paradigm.

Experimental Section

Fabrication of the Hybrid Cell: For the sliding part, the Al foil connected with a wire was pasted on an acrylic board to ensure it is flat on the surface. For the static part, first one side of a PTFE film and both sides of a polarized PVDF film (both commercially available) were deposited with Cu thin film layers, respectively. To be used as electrodes, all these Cu layers were connected with wires individually. Then the top surface of the PVDF with the polarization direction pointed out was placed with a layer of Kapton double-side tape, and the other side of the tape was pasted

on the side of the PTFE film with the Cu layer. Finally, the other side of the PVDF was pasted on another acrylic board to be the static part. A groove was engraved on the acrylic board of the static part by the laser for inserting a thermocouple.

Setups of the Measurement of the Hybrid Cell: The sliding part was fixed on a linear motor with the Al foil side downward and the static part was fixed on a 3D stage with the PTFE side upward. The height of the static part was adjusted by the stage to ensure the Al and the PTFE surfaces were firmly contacted with existence of the normal force. The linear motor was controlled to move forward/backward periodically with a period of 0.2267 s. The voltages and the currents were measured by a Keithley 6514 system electrometer, and the temperature was recorded by the thermocouple.

Fabrication and Capacitance Measurement of the Supercapacitor: The supercapacitor included two identical ruthenium dioxides (RuO_2) on titanium (Ti) substrates as the cathode and the anode, respectively, with porous polyethylene (PE) film as the separator and $1 \text{ M H}_3\text{PO}_4$ aqueous solution as the electrolyte. The RuO_2 electrodes were in situ synthesized on the Ti substrates via a vapor phase hydrothermal route. The supercapacitor was sealed with polydimethylsiloxane (PDMS) between two Kapton films. The capacitance of the supercapacitor was tested on EC-Lab (Princeton applied research, VersaSTAT 3) by using electrochemical impedance spectroscopy (EIS) technique at the frequency of 10 mHz.

Fabrication and Measurement Setups of the Hybrid Cell as Sensors: The fabrication process of the disc 2 was similar to that of the static part in the hybrid cell, except the acrylic board was cut to be a round shape (diameter: 4 in.) and three small PVDF pieces were pasted as described in the article. The disc 1 covered with a layer of Al foil was also cut to be a round shape with the same size. In the measurement for the temperature sensing, the disc 1 was connected with a rotation motor and the disc 2 was fixed in a 3D stage. The position of the disc 2 was adjusted by the stage to ensure the PTFE side of the disc 2 contact with the Al foil side of the disc 1 firmly. In the measurement for the normal force sensing, a force meter was connected with a linear motor, perpendicular to the disc 2 fixed on the stage. The position of the disc 2 was controlled to make sure the tip of the force meter was 4.9 mm away from the PPENG #3 and they were in the same height. The linear motor was controlled to move forward/backward periodically with a period of about 2.1 s. The displacements from 5 to 5.8 mm were set to create different applied forces. All the electrical and temperature measurement methods were kept identical.

Supporting Information

Supporting Information is available from the Wiley Online Library or from the author.

Acknowledgements

Y.Z. and L.L. contributed equally to this work. This work was supported by the U.S. Department of Energy, Office of Basic Energy Sciences (DE-FG02-07ER46394), the Hightower Chair foundation, and the “thousands talents” program for pioneer researcher and his innovation team, China, National Natural Science Foundation of China (Grant No. 51432005), Beijing City Committee of Science and Technology (Z131100006013004, Z131100006013005).

Received: January 9, 2015

Revised: January 28, 2015

Published online:

[1] Z. L. Wang, *Sci. Am.* **2008**, 298, 82.

[2] Z. L. Wang, W. Wu, *Angew. Chem. Int. Ed.* **2012**, 51, 11700.

[3] Z. L. Wang, J. Song, *Science* **2006**, 312, 242.

- [4] Y. Hu, Z. L. Wang, *Nano Energy* **2014**, DOI: 10.1016/j.nanoen.2014.11.038.
- [5] E. S. Nour, A. Khan, O. Nur, W. Magnus, *Nanomater. Nanotechnol.* **2014**, DOI: 10.5772/59068.
- [6] F.-R. Fan, Z.-Q. Tian, Z. L. Wang, *Nano Energy* **2012**, *1*, 328.
- [7] Z. L. Wang, *ACS Nano* **2013**, *7*, 9533.
- [8] Z. L. Wang, *Faraday Discuss.* **2014**, DOI: 10.1039/C4FD00159A
- [9] S. Wang, Y. Xie, S. Niu, L. Lin, Z. L. Wang, *Adv. Mater.* **2014**, *26*, 2818.
- [10] L. Lin, S. Wang, S. Niu, C. Liu, Y. Xie, Z. L. Wang, *ACS Appl. Mater. Interfaces* **2014**, *6*, 3031.
- [11] S. Wang, L. Lin, Y. Xie, Q. Jing, S. Niu, Z. L. Wang, *Nano Lett.* **2013**, *13*, 2226.
- [12] G. Zhu, J. Chen, Y. Liu, P. Bai, Y. S. Zhou, Q. Jing, C. Pan, Z. L. Wang, *Nano Lett.* **2013**, *13*, 2282.
- [13] S. Niu, Y. Liu, S. Wang, L. Lin, Y. S. Zhou, Y. Hu, Z. L. Wang, *Adv. Mater.* **2013**, *25*, 6184.
- [14] M. G. Broadhurst, G. T. Davis, J. E. McKinney, R. E. Collins, *J. Appl. Phys.* **1978**, *49*, 4992.
- [15] H. L. W. Chan, P. K. L. Ng, C. L. Choy, *Appl. Phys. Lett.* **1999**, *74*, 3029.
- [16] T. Furukawa, N. Seo, *Jpn. J. Appl. Phys.* **1990**, *29*, 675.
- [17] X. Li, S.-G. Lu, X.-Z. Chen, H. Gu, X.-S. Qian, Q. M. Zhang, *J. Mater. Chem. C* **2013**, *1*, 23.
- [18] R. G. Kepler, R. A. Anderson, *J. Appl. Phys.* **1978**, *49*, 4490.
- [19] Q. Leng, L. Chen, H. Guo, J. Liu, G. Liu, C. Hu, Y. Xi, *J. Mater. Chem. A* **2014**, *2*, 11940.
- [20] J.-H. Lee, K. Y. Lee, M. K. Gupta, T. Y. Kim, D.-Y. Lee, J. Oh, C. Ryu, W. J. Yoo, C.-Y. Kang, S.-J. Yoon, J.-B. Yoo, S.-W. Kim, *Adv. Mater.* **2014**, *26*, 765.
- [21] K. L. Bing, T. Li, H. H. Hng, F. Boey, T. Zhang, S. Li, *Waste Energy Harvesting: Mechanical and Thermal Energies*, Springer, Berlin, **2014**.
- [22] Y. Yang, S. Wang, Y. Zhang, Z. L. Wang, *Nano Lett.* **2012**, *12*, 6408.
- [23] K. Lefki, G. J. M. Dormans, *J. Appl. Phys.* **1994**, *76*, 1764.
- [24] G. Zhu, Y. S. Zhou, P. Bai, X. S. Meng, Q. Jing, J. Chen, Z. L. Wang, *Adv. Mater.* **2014**, *26*, 3788.
- [25] G. Zhu, J. Chen, T. Zhang, Q. Jing, Z. L. Wang, *Nat. Commun.* **2014**, DOI: 10.1038/ncomms4426.
- [26] C. Birlikseven, E. Altıntaş, H. Zafer Durusoy, *J. Mater. Sci.: Mater. Electron.* **2001**, *12*, 601.